Internal load transfer and damage evolution in a 3D interpenetrating metal/ceramic composite

Siddhartha Roy, Jens Gibmeier, Vladimir Kostov, Kay A. Weidenmann, Alwin Nagel, Alexander Wanner

Angaben zur Veröffentlichung / Publication details:

Roy, Siddhartha, Jens Gibmeier, Vladimir Kostov, Kay A. Weidenmann, Alwin Nagel, and Alexander Wanner. 2012. "Internal load transfer and damage evolution in a 3D interpenetrating metal/ceramic composite." *Materials Science and Engineering: A* 551: 272–79. https://doi.org/10.1016/j.msea.2012.05.016.

Internal load transfer and damage evolution in a 3D interpenetrating metal/ceramic composite

Siddhartha Roy[a,*], Jens Gibmeier[a], Vladimir Kostov[a], Kay André Weidenmann[a], Alwin Nagel[b], Alexander Wanner[a]

[a] *Institute for Applied Materials, Karlsruhe Institute of Technology, 76131 Karlsruhe, Germany*
[b] *Hochschule Aalen, Beethovenstr. 1, 73430 Aalen, Germany*

1. Introduction

Metal matrix composites (MMC) typically exhibit for example higher specific stiffness and strength, better creep and wear resistance etc. in comparison to the monolithic metallic matrix [1]. The strength of an MMC depends upon the extent of indirect and direct strengthening. Indirect strengthening results from the generation of lattice dislocations at the matrix-reinforcement interface, and their mutual interaction [2,3]. Direct strengthening occurs due to internal load transfer from the metallic matrix to the stiffer and stronger reinforcement [4]. The extent of load transfer depends upon the volume fraction, shape and orientation of the reinforcing phase, as well as the elastic mismatch between the two phases [5]. For an MMC to behave in an efficient manner, the reinforcement phase needs to carry the highest possible fraction of the load, without itself getting damaged.

Lattice diffraction-based techniques are ideal to analyse the internal load transfer mechanism in MMCs, as they allow stress analysis in all crystalline phases present in the microstructure. A number of studies have used either neutron [5–11] or synchrotron X-ray [4,12–18] diffraction to study the internal load transfer mechanism in MMCs. An excellent review of such work has recently been published [19]. Both these techniques allow analysis to be carried out in the bulk of the material, however with substantially different spatial resolutions. In an earlier study, we analysed the internal load transfer mechanism under external tension and compression in a three dimensionally interpenetrating Al_2O_3/AlSi12 composite using energy dispersive synchrotron X-ray diffraction (EDXRD) [20]. In depth analysis of the interplanar anisotropy as well as the internal load transfer was carried out in two separate samples under monotonic loading conditions.

The aim of the present study is to gain further insight into the load transfer mechanism and damage evolution in this composite material. Hence, internal load transfer during a complete loading path starting in compression followed by unloading and reloading in tension until fracture was investigated. Lattice strains in all three phases (alumina reinforcement, silicon and aluminium solid solution) along the directions parallel and transverse to that of the applied load were measured at several constant applied stress levels using EDXRD. Lattice strain evolution in several (up

* Corresponding author.
E-mail address: siddhartha.roy@kit.edu (S. Roy).

to 7) diffraction planes of each phase was analysed, ensuring that the calculated average strains and stresses were reliable and representative of the material behaviour. Additionally, lattice strain analysis during the loading path starting in compression followed by unloading and reloading in tension allows identifying the occurrence of the Bauschinger effect in aluminium and damage within alumina phase. Knowledge about the extent of the observed Bauschinger effect is important for the assessment of cyclic loading behaviour of the composite. For a more direct analysis of progressive damage behaviour, one composite sample with similar ceramic content was further compressed in situ in a scanning electron microscope (SEM) and images were captured at different applied stress levels.

2. Experimental procedure

2.1. Specimen material

The composite material was fabricated by the Materials Research Team of Aalen University of Applied Sciences, Germany, following a processing route thoroughly described in Refs. [20,21]. Commercially available alumina powder was first mixed with cellulose fibres used as a pore forming agent. The powder mixture was uni-directionally compressed under 100 MPa applied pressure into plates and then sintered in an electrically heated tube furnace under an oxidising atmosphere. The sintering temperature was 1550 °C and during this process pyrolysis of the pore forming agents also occurred. The porous preforms were subsequently infiltrated with a eutectic aluminium–silicon (AlSi12) melt via direct squeeze-casting under 100 MPa pressure along the same direction as that of powder pressing before sintering.

2.2. Experimental procedure

EDXRD measurements were carried out at the materials science beamline EDDI at the Berlin synchrotron source BESSY, Germany. Detail technical specifications of the beamline components are described in [22]. Only a brief description of the diffraction experiment is given here and for thorough description we refer to an earlier publication [20]. The sample had a 10 mm uniform gauge length in the middle and a 5 mm gauge diameter. A scattering angle $2\theta = 10.27^\circ$ was chosen as it gave good energy separation as well as sufficient peak intensities. The load applied to the sample was increased stepwise and at each stress step diffraction measurement were carried out following the $\sin^2\psi$ method [23] by stepwise tilting the test set-up between $\psi = 0^\circ$ and $\psi = 89.9^\circ$. The sample was loaded according to the following stress steps (in MPa): $0 \rightarrow -102 \rightarrow -198 \rightarrow -298 \rightarrow -203 \rightarrow -104 \rightarrow -2 \rightarrow 96 \rightarrow 196 \rightarrow$ breakage. Slits in the paths of the incoming and outgoing beam resulted into a nominal gauge volume of 0.3 mm^3 inside the sample. Individual diffraction lines from the EDXRD spectra were fitted by a "Pseudo-Voigt" function to determine the line positions. It is possible to determine lattice strains by calculating the shifts of the diffraction lines according to:

$$\varepsilon = \frac{d^{hkl}}{d_0^{hkl}} - 1 = \frac{E_0^{hkl}}{E^{hkl}} - 1 \quad (1)$$

where d_0^{hkl} and E_0^{hkl} are the lattice plane spacings and the energy peak positions of the $\{hkl\}$ family of planes in the unstressed condition, respectively.

In situ compression test of one composite sample was carried out inside an SEM to study the progressive damage behaviour. The sample had dimensions of $2.8 \times 2.64 \times 2.73\ mm^3$, and it was compressed along the direction of preform pressing and squeeze-casting. The sample was compressed between two hardened steel punches in a miniature mechanical testing machine manufactured by Kammrath and Weiss GmbH (Dortmund, Germany). 20 μm thick Al foils were placed between the sample and the punches to reduce frictional effects at the contact surfaces. The compression test was carried out at a crosshead velocity of 2 μm/s.

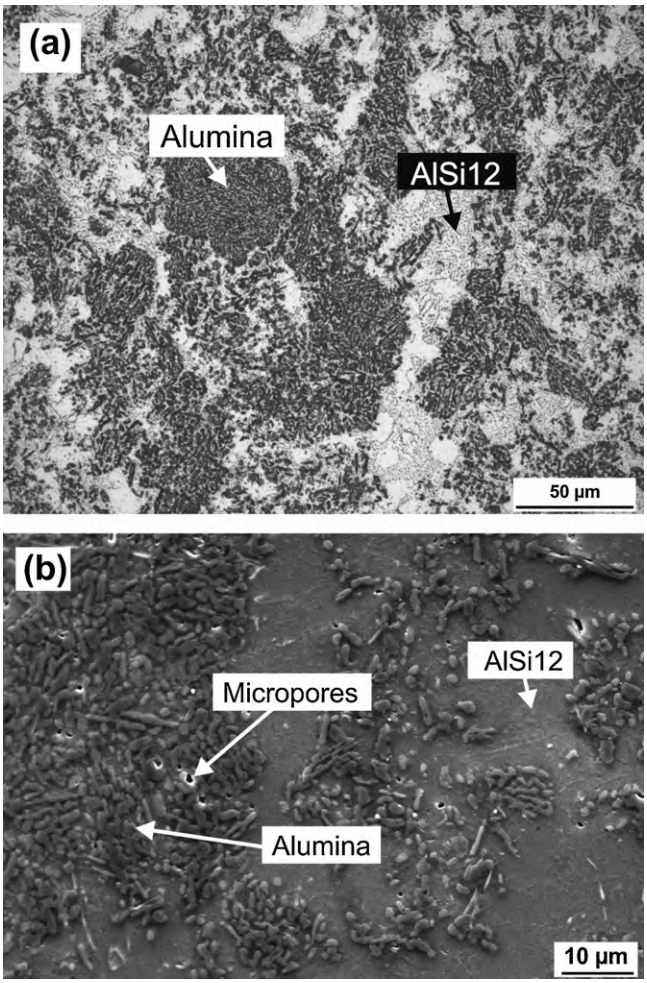

Fig. 1. Micrographs of the studied composite material for the face perpendicular to the direction of perform pressing and squeeze-casting (a) light optical micrograph and (b) SEM micrograph.

Reprinted from "S. Roy, J. Gibmeler, V. Kostov et al., Internal load transfer in a metal matrix composite with a three-dimensional interpenetrating structure, Acta Materialia, 59 (14) (2011) 24–1435, with permission from Elsevier."

3. Results and discussions

3.1. Structural analysis

Fig. 1 shows typical microstructures of the studied composite for the face perpendicular to the direction of preform pressing and squeeze-casting. Fig. 1a shows a light-optical micrograph while Fig. 1b shows a micrograph taken with an SEM. Features of the composite microstructure are described in earlier publications [20,24] and are not further discussed here. The composite consists of three phases–alumina reinforcement (dark grey regions in the optical micrograph), aluminium solid solution and pure silicon particles distributed randomly within the aluminium solid solution. The SEM micrograph in Fig. 1b shows that the alumina-rich regions are not densely packed, and they are composed of individual alumina

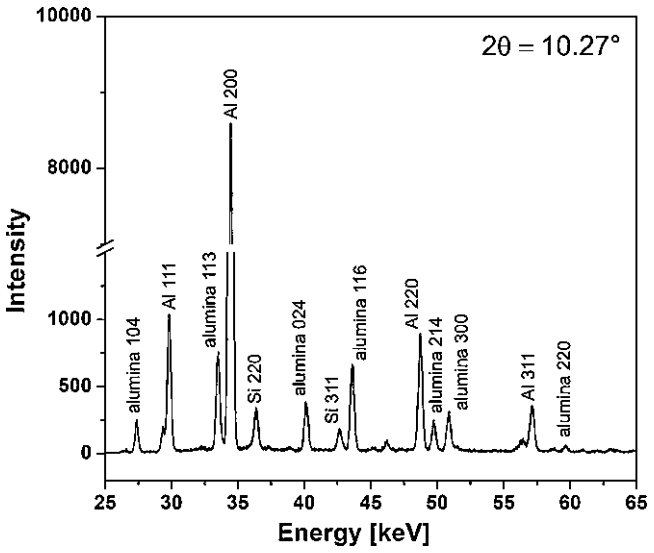

Fig. 2. Typical EDXRD spectrum obtained from the AlSi12–Al_2O_3 MMC acquired using a diffraction angle of 10.27°. Indexed diffraction planes of each phase are marked in the spectrum.

particles with metallic alloy between them. While the macropores of the preform were completely infiltrated, the pores between the alumina particles in the ceramic wall remained partially uninfiltrated, giving rise to residual microporosity in the composite. These residual micropores are marked in Fig. 1b.

The density of the sample studied for load transfer analysis was determined according to the Archimedes' principle, while the density of the sample used to study the compressive damage evolution was determined from its mass and dimensions only. Densities of the two samples were 3.065 Mg/m^3 and 3.15 Mg/m^3, respectively. Neglecting porosity and using the bulk densities of alumina and AlSi12 (density of alumina was taken as 3.90 Mg/m^3 [25] while the density of AlSi12 was measured in an earlier study as 2.66 Mg/m^3 [24]), the ceramic contents in the samples were determined as 33 vol% and 40 vol%, respectively. However, residual porosity, resulting from differential thermal contraction of the two phases after infiltration, may shift the calculated alumina content in the sample to approximately 0.7 vol% higher [20].

3.2. Evolution of lattice microstrain

Fig. 2 shows typical EDXRD spectrum for the studied AlSi12/Al_2O_3 composite acquired using a diffraction angle of 10.27°. Seven diffraction planes of alumina (namely {1 0 4}, {1 1 3}, {0 2 4}, {1 1 6}, {2 1 4}, {3 0 0} and {2 2 0}), 4 diffraction planes of Al (namely {1 1 1}, {2 0 0}, {2 2 0} and {3 1 1}) and 2 diffraction planes of Si (namely {2 2 0} and {3 1 1}) were analysed. As discussed in Ref. [20], at each applied stress step, d vs. $\sin^2\psi$ plots were created for each indexed plane. Best-fit straight lines over the complete $\sin^2\psi$ range between 0 and 1 were calculated for each individual distribution. For the present experiment, the diffraction vector was almost parallel to the loading direction for $\sin^2\psi = 0$ and it was almost transverse to the loading direction for $\sin^2\psi = 1$. Hence, the d-spacings determined from the equations of the best-fit lines were used as the d-spacings parallel and transverse to the loading direction, respectively. As a result of this followed methodology, the resultant d-spacings used for the lattice strain calculation were statistically more reliable in comparison to the experimentally determined d-spacings at only the two extreme ψ-tilts of $\psi = 0°$ and $\psi = 90°$.

Fig. 3 shows the evolution of the continuum mechanics average lattice strain in all three phases of the MMC as a function of applied stress. The plots on the left hand side correspond to the loading direction, while the plots on the right hand side show the microstrains transverse to the loading direction. While calculating the lattice strains, processing-induced thermal residual stresses were neglected, and the strains were calculated with respect to the initial 'as processed' state at zero applied stress. Hence, reported lattice strains are the changes with respect to this initial state. Here onwards, only "lattice strain" will be used to denote this change. Our previous study [20] on internal load transfer under external tension and compression in the same composite material showed that plastic yielding in the aluminium phase began at similar applied stress level, suggesting that processing induced residual stresses do not play a significant role in the studied composite. Although, lattice strain evolution in several planes of each phase was measured, they are not shown here for the sake of clarity. Study of lattice strain evolution in several planes of each phase allows understanding the extent of interplanar anisotropy and this has been discussed in detail for the studied composite under monotonic external tension and compression in Ref. [20]. The continuum mechanics average lattice strain in each phase was calculated following the method described by Daymond [26], using the multiplicity factor of each diffracting plane and assuming the absence of any texture (texture factor taken as unity) as a first approach. In all the figures the error bars correspond to the standard deviation of the lattice strains among all the indexed diffraction planes of each phase and they mirror the phase specific interplanar anisotropy to some extent.

To begin with, in all three phases the compressive lattice strain along loading direction increase with increasing applied compressive stress. At applied compressive stresses higher than 100 MPa, the rate of increase of lattice strain with applied stress decreases in aluminium. This results from the plastic deformation of aluminium and corresponding load transfer to alumina and silicon at higher stresses. Correspondingly, the curves of silicon and alumina show a reduced slope. This change in load transfer characteristics caused by initiation of plastic deformation in aluminium under external monotonic tension and compression has been thoroughly described in Ref. [20]. Due to its higher stiffness in comparison to silicon, a higher fraction of the load is transferred to alumina and hence, the change of slope at higher applied compressive stresses is more prominent in alumina. During unloading, until 100 MPa applied compressive stress, the slope of the curve for aluminium is similar to the slope of the initial portion of the loading curve. This suggests that during unloading, aluminium is behaving elastically until this point. During further unloading to zero applied stress, the slope of the curve for aluminium again increases, suggesting initiation of plastic yielding in tension and reoccurrence of the load transfer. During unloading, zero microstrain in aluminium is reached at an applied compressive stress of approximately 125 MPa. Thus, the slope change occurring in aluminium at an applied compressive stress of 100 MPa during unloading indicates the occurrence of the Bauschinger effect. The Bauschinger effect is a phenomenon which commonly occurs in ductile metals and it manifests itself as an earlier initiation of plastic flow during reverse loading in comparison to the immediately preceding forward loading step [27]. According to Orowan [28], this results from the lesser effective barrier to dislocation motion during reverse flow than during the forward flow and is often discussed for being affected by local micro residual stress fields. Several studies have shown that the presence of elastic inclusions results in significant Bauschinger effect in MMCs [29–31]. The extent of the Bauschinger effect has been reported to be strongly dependent on the characteristics of the metallic matrix and the reinforcement – the extent increases with increasing reinforcement aspect ratio and volume fraction, while being relatively insensitive to the strain hardening exponent of the metallic matrix [30]. Strain hardening exponent of AlSi12 in the current study was determined from its tensile true

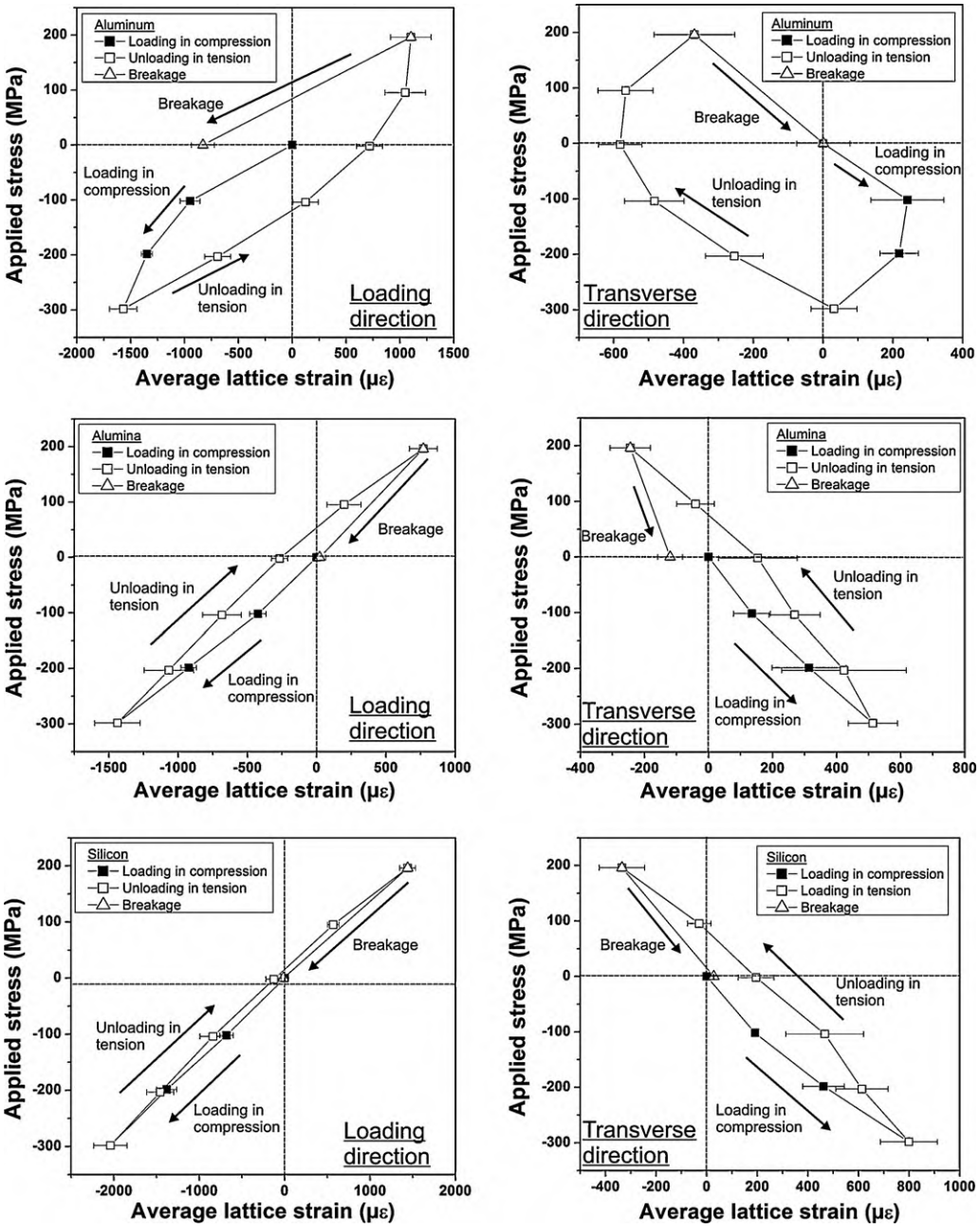

Fig. 3. Evolution of the continuum mechanics equivalent lattice strain along (plots on the left hand side) and transverse (plots on the right hand side) to the loading direction in all three phases of the composite as a function of the applied stress.

stress-true strain plot, by fitting a straight line between the 0.2% yield stress and the tensile strength and its value was found to be 0.31. Aspect ratio of alumina particles was determined by measuring the ratio of the small and long half axes of several particles in Figure 1 and they lie in the range of 0.2 and 0.63 with a mean value of 0.3 [32]. The extent of the Bauschinger effect needs to be considered when the composite is put under service involving alternating stresses. A pronounced Bauschinger effect may initiate premature plastic deformation in the metallic alloy during reverse loading, thus damaging the structural integrity of the composite. For a thorough and systematic investigation of the influence of these factors on the extent of the Bauschinger effect in the current material, several different alumina/Al alloy composites must be studied, which was outside the scope of this work.

After complete unloading to zero applied stress, the residual lattice strains are tensile in aluminium and they are compressive in alumina and silicon. Upon loading the sample in tension through fracture, the lattice strain in aluminium is compressive due to prior tensile plastic deformation, while the lattice strains in both silicon and alumina are zero.

Initially, the transverse lattice strain in all three phases also increases with increasing applied stress. However, the sign of the transverse lattice strain is opposite to the lattice strain along the loading direction due to Poisson's effect. At applied compressive stresses higher than 100 MPa, the transverse lattice strain in aluminium suddenly changes its trajectory, and tends to become compressive. This is caused by the sudden change of the Poison's ratio of aluminium resulting from initiation of plastic deformation and has been discussed in detail in earlier publications [18,20]. During unloading, the transverse lattice strain curves for all three phases display elastic behaviour within experimental uncertainties until 100 MPa applied compressive stress. At the instance of

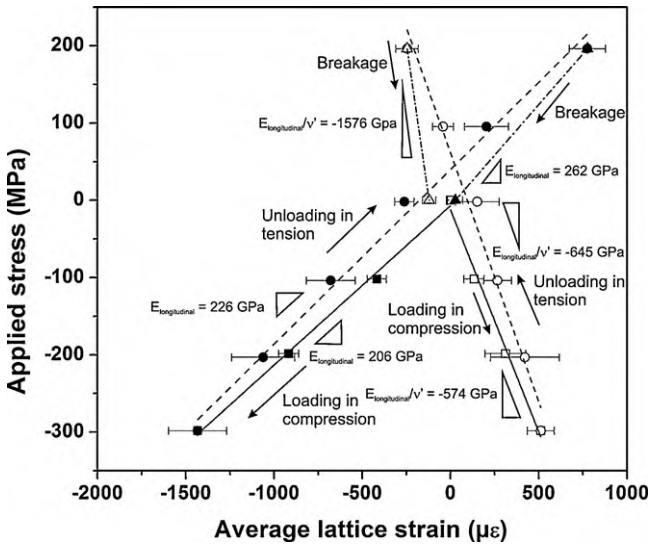

Fig. 4. Evolution of $E_{\text{longitudinal}}$ and $E_{\text{longitudinal}}/\nu'$ of alumina during the complete loading path.

complete unloading, the transverse microstrain is compressive in aluminium, and tensile in silicon and alumina. With continued loading in tension, the transverse lattice strain profile of alumina and silicon display the expected trend, however, the profile for aluminium again changes its trajectory due to the elastic–plastic Poisson's ratio mismatch.

Slope of the applied stress vs. average lattice strain along loading direction may be defined as the longitudinal *E*-modulus ($E_{\text{longitudinal}}$). The corresponding slope when strain is measured transverse to the loading direction is equal to the quantity $E_{\text{longitudinal}}/\nu'$, where ν' is the Poisson's ratio for the actual stress state within the material. The evolution of $E_{\text{longitudinal}}$ and $E_{\text{longitudinal}}/\nu'$ are shown in Fig. 4 for both loading paths. For each path and for both longitudinal and transverse directions, a best-fit straight line is drawn in the plot of applied stress vs. lattice microstrain, and the slope of this best fit line is used as the two quantities. For the first loading in compression, $E_{\text{longitudinal}} = 206$ GPa and $E_{\text{longitudinal}}/\nu' = -574$ GPa. The value of the longitudinal modulus is almost half that of pure alumina ($E = 390$ GPa). This is due to the load transfer occurring from plastically deforming aluminium. Fig. 4 further shows that during unloading in tension and after breakage of the sample, the values of both $E_{\text{longitudinal}}$ and $E_{\text{longitudinal}}/\nu'$ increase. An increase in *E*-modulus of alumina corresponds to a decrease in the load carried by this phase, an effect probably caused by damage of the alumina phase. Using effective stress concept and strain equivalence principle, Lemaitre [33] showed that following elasticity law, the stiffness of a material decreases with increasing damage accumulation in it. This idea has been used in several studies to derive a damage parameter in metal matrix composites by measuring the unloading *E*-modulus at various applied stresses during a tensile test [34,35].

3.3. Calculation of phase stress from lattice microstrain

Average phase stress along the loading direction (named as longitudinal phase stress here onwards) can be calculated from the measured longitudinal and transverse elastic lattice strains following the equation [27]:

$$\sigma_1 = \frac{E}{1+\nu}\varepsilon_1 + \frac{\nu E}{(1+\nu)(1-2\nu)}(\varepsilon_1 + \varepsilon_2 + \varepsilon_3) \quad (2)$$

In this equation σ_1 is the calculated longitudinal phase stress, ε_1 is the average lattice strain in each phase along the loading direction, $\varepsilon_2 = \varepsilon_3$ are the average lattice strains in each phase along transverse directions and E and ν are the *E*-modulus and the Poisson's ratio, respectively. Macroscopic *E*-modulus and Poisson's ratio of each phase, used as E and ν are given in Table 1 [36,37]. As the change in lattice strain with respect to step 1 has been used to determine the longitudinal phase stress, the determined stress in reality denotes only the change with respect to this initial state. In the following, "longitudinal phase stress" will be used to refer to this change. Eq. (2) is based on the assumption that the individual phases of the composite are elastically isotropic. As discussed in [20], this assumption although justified for alumina and aluminium, may result in significant errors in the calculated longitudinal stress in silicon.

Table 1
Macroscopic elastic constants for the three phases of the MMC used to calculate the longitudinal phase stress from the measured lattice strain.

	Poisson's ratio (ν)	*E*-modulus (E in GPa)
Alumina	0.24	390
Aluminium	0.351	69.9
Silicon	0.22	163

Fig. 5 shows the longitudinal phase stress (σ_1) in each phase of the composite calculated as discussed above, vs. the applied stress. During loading in compression, at applied compressive stresses higher than 100 MPa, the slope of the curve for aluminium decreases and that of alumina slightly increases resulting from the internal load transfer. After unloading from the compression half cycle, σ_1 is tensile in aluminium, and it is compressive in alumina. For the same applied stress during both loading and unloading, the σ_1 values in silicon superimpose on each other. Phase stress concentration factor may be defined as the ratio of the longitudinal phase stress and the applied stress [20]. The thick grey line in each plot in Fig. 5 denotes a guideline having a slope = 1, and along this line the longitudinal phase stress in each phase equals the applied stress (i.e. phase stress concentration factor = 1). The plots clearly show that the value of this factor for aluminium is always less than one due to load transfer. In alumina, at the highest applied compressive stress, this ratio is approx. 1.7 while, after unloading in tension and at the highest achieved tensile stress step just before breakage, the ratio changes to approx. 1.4. Decrease of this factor during unloading and reloading in tension denotes occurrence of damage in alumina. Throughout, the stress concentration factor in silicon remains close to unity, suggesting that only marginal load transfer occurs within the metallic alloy itself.

Fig. 5 shows that after tensile fracture σ_1 is nearly zero in alumina, while it is compressive in aluminium. Hence, the condition of stress balance is not fulfilled. According to this condition the sum of the product of σ_1 and volume fraction (V_f) in each phase ($\sum(\sigma_{1,f}V_f)$) must be equal to the applied external stress. As the calculated stresses denote changes with respect to the initial unloaded state, after sample fracture $\sum(\sigma_{1,f}V_f) \sim 0$ must be fulfilled. To study the deviation between the applied (σ_{applied}) and calculated total stress ($\sigma_{\text{calculated}}$), $|(\sigma_{\text{applied}} - \sigma_{\text{calculated}})|$ is plotted against σ_{applied} in Fig. 6. The plot shows that until complete unloading following initial compression, the deviation is relatively low and within experimental uncertainties. However, with continued loading in tension the deviation increases, reaching a maximum after sample fracture. Comparison between Fig. 4 and Fig. 6 shows that this deviation increases with increasing *E*-modulus, and hence probable damage of alumina. Due to the very heterogeneous structure of the composite, once damage initiates, the stress state within the composite becomes rather complex and spatially inhomogeneous. Due to the small sizes of the incoming and the outgoing slits during diffraction measurement, the diffraction gauge

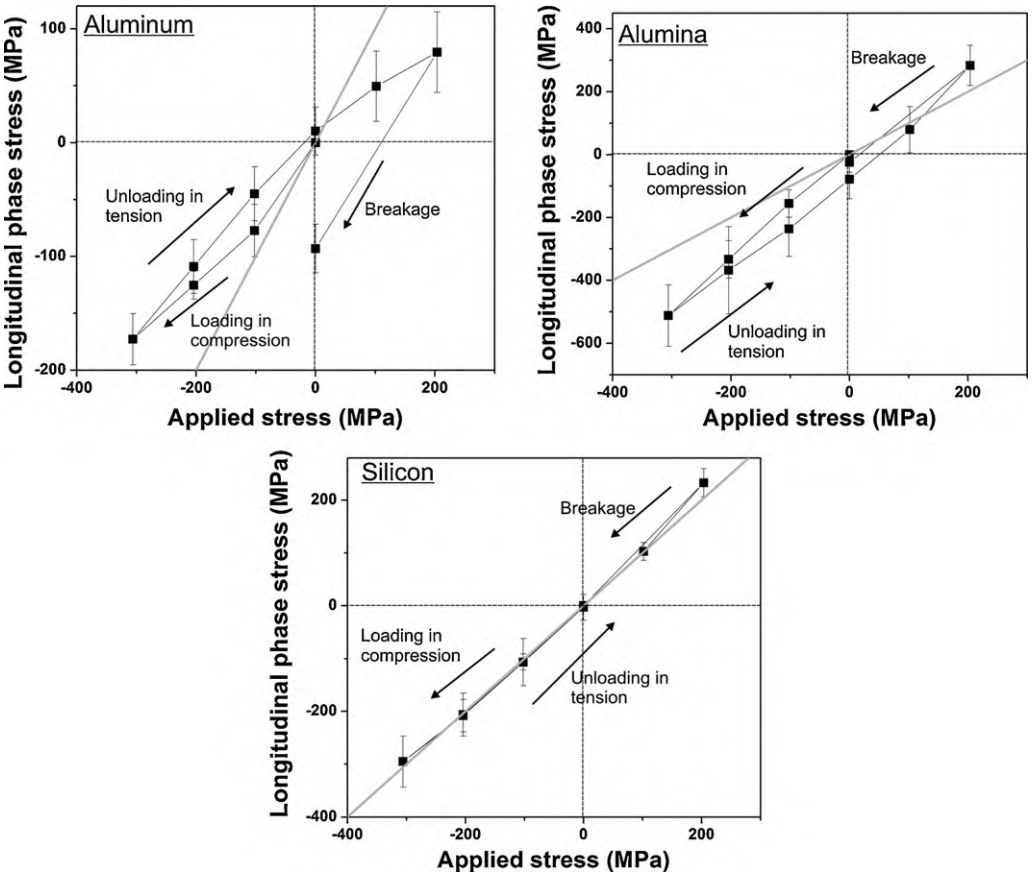

Fig. 5. Plot of longitudinal phase stress vs. applied stress for the three phases of the composite. The thick grey line in each plot corresponds to a stress concentration factor = 1.

volume had the shape of an elongated rhombohedron (nominal dimensions 5.1 mm × 1 mm × 0.06 mm), which was not representative of the whole sample. Hence, it is possible that localised stresses exist at regions surrounding the gauge volume to fulfil the condition of stress balance, which however has not been measured in diffraction. To obtain a more representative stress state for the whole sample, the diffraction gauge volume should be chosen to integrate the stress distribution over the complete gauge diameter of the sample. This cannot be satisfied with high-energy synchrotron diffraction at relatively small diffraction angles, but might be realised e.g. with neutron time of flight measurements, albeit at a much higher acquisition time.

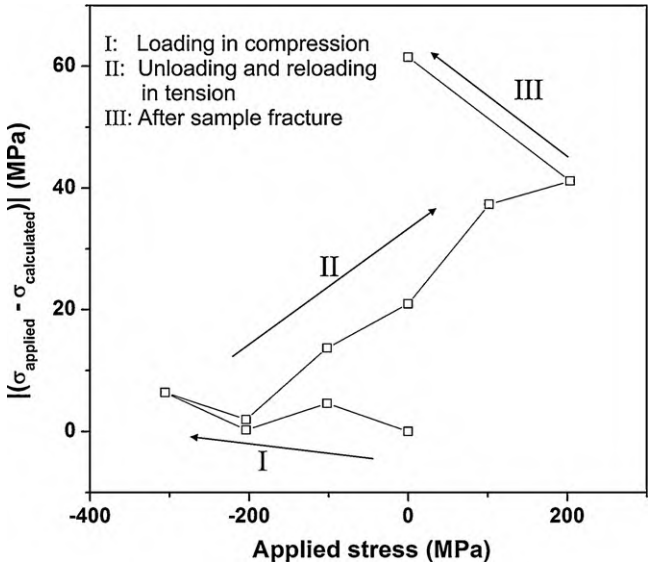

Fig. 6. Plot of the absolute deviation between applied and calculated total stress vs. applied stress.

3.4. *In situ study of progressive damage evolution under external compression*

Considering the significant influence of the inhomogeneous microstructure and damage evolution on internal load transfer, in situ study of the progressive damage mechanism of the composite is of special interest. This study was carried out for one sample with 40 vol% nominal ceramic content under external compression in situ inside an SEM. Fig. 7a–c shows the progressive compressive damage behaviour in a representative region of the sample. The sample was compressed along the horizontal direction in these images. The compressive strength of the sample was 558 MPa. Fig. 7a shows the microstructure of the sample at an applied stress of 7 MPa. The microstructure of the same region of the sample at 544 MPa is shown in image b, while the image after sample fracture is shown in image c. Image b shows that cracking starts within the ceramic rich region and the crack is oriented at approximately 45° to the compression axis. This crack subsequently propagates at higher applied stresses to cause final fracture of the sample. Image c shows that the long crack is also oriented at approximately 45° with the loading axis, and it propagates preferentially through the ceramic rich regions. Propagation of damage is very heterogeneous, with regions further away from the main crack showing limited or no damage.

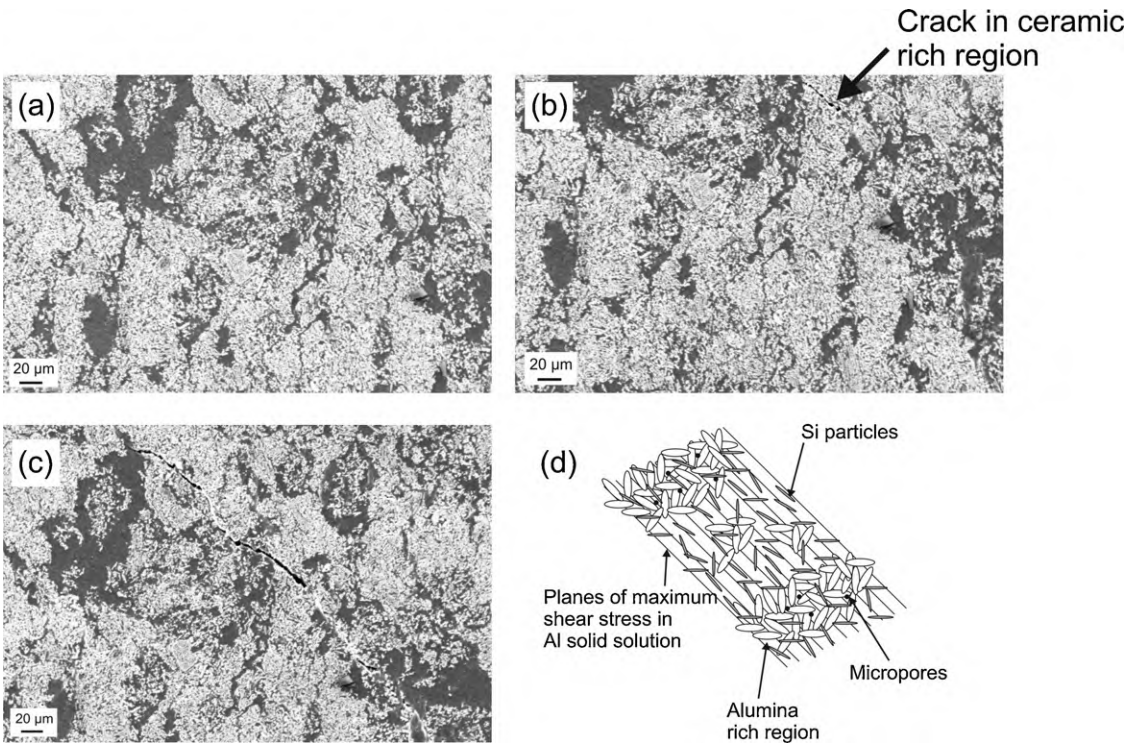

Fig. 7. Scanning electron micrographs showing progressive compressive damage evolution in one region within a sample with nominal ceramic content 40 vol%. Compression was carried out along the horizontal direction. (a) At applied stress = 7 MPa, (b) applied stress = 544 MPa, (c) after final fracture and (d) schematic image showing planes of maximum share stress in Al solid solution. In the micrographs the ceramic phase is bright while the metallic region is darker.

Deformation and damage mechanism of the composite may be explained in light of the particle reinforced MMCs with non-uniform particle distribution [29,38–40]. Fig. 7d schematically shows the different features of the deformed microstructure of the interpenetrating composite for a projection in 2D. This is a modified version of the schematic image proposed by Wang and Zhang [29] for damage in particle reinforced MMCs. Straight lines in this image, oriented at 45° to the loading direction denote the planes of maximum shear stress in aluminium solid solution. Under the application of external stress, load is transferred from the ceramic free regions to ceramic rich regions [38]. Plastic flow in Al solid solution within the ceramic rich regions would however be strongly interrupted by the presence of the stiffer, harder and non-deformable alumina (and also silicon particles to some lesser extent) particles. This will give rise to high tri-axial stress within the Al solid solution in this region, which would crack the metallic phase and would propagate further through the highly stressed regions. Micropores present within the composite may also act as crack initiators. As shown in Fig. 1b, the micropores are present only within the ceramic rich regions. Such micropores within particle clusters have already been reported in particle reinforced MMCs [41], and they have been reported to act as crack initiators under external stress [42].

4. Conclusions

Internal load transfer in a 3D interpenetrating metal/ceramic composite was studied using energy dispersive synchrotron X-ray diffraction. The chosen diffraction technique allows multiple diffraction peaks of all contributing crystalline phases of the composite to be analysed. Due to the small gauge volume, measurements can be carried out with high spatial resolution; however, in case of complex microstructures, as in the composite studied in this work, this may indeed be a limitation as the stress state within the diffraction gauge volume (which for the applied small diffraction angles has the shape of an elongated rhombohedron) may be very different from the overall average. Measurements were carried out at different applied stresses during one compression-tension until failure path in transmission mode according to the $\sin^2\psi$ method of X-ray stress analysis. Multiple diffraction peaks in all three phases of the composite were analysed. Compressive damage evolution was studied in situ in a scanning electron microscope. The following main conclusions are drawn:

- Load reversal after initial compression results into significant Bauschinger effect within aluminium. This bears significance for cyclic loading of the composite material. For a thorough understanding of the influence of the structural parameters on the Bauschinger effect, composites with different ceramic contents and with varying microstructures need to be studied.
- The measured longitudinal *E*-modulus of alumina in the composite is almost half of pure alumina during initial loading. During further unloading and subsequent reloading in tension, the stress concentration factor in alumina decreases and the longitudinal *E*-modulus increase due to progressive damage of the alumina phase.
- In situ SEM compression test shows that damage occurs by propagation of cracks through the metallic alloy within the ceramic rich regions. Due to the constriction of the stiffer and harder alumina particles, plastic flow within the metallic phase is strongly interrupted in these regions. This will give rise to strong tri-axial stresses in the metallic phase, which subsequently causes failure.

Due to the challenge posed by the complex interpenetrating structure, the mechanical properties of interpenetrating MMCs have been studied to a lesser extent in comparison to fibre and particle reinforced composites. Apart from being almost isotropic, these MMCs display a good combination of strength, toughness and

wear resistance and it is also possible to vary the phase architecture over wide ranges to fabricate tailor-made structures. Effect of phase architecture as well as the processing parameters on the load transfer mechanism will be studied in our future works.

Acknowledgements

We thank the synchrotron radiation facility BESSY (Berlin, Germany) for granting us beamtime under the proposal 2009_2_90335 and the EDDI beamline staff for their excellent technical assistance. The authors also thank Mr. Kabelo Sebetlela (IAM-WK, KIT) for his assistance in in situ compression test. Co-author SR thanks German Research Foundation (DFG) for financial assistance within the project RO 4164/1-1 for the period of preparation of the manuscript.

References

[1] N. Chawla, K.K. Chawla, Metal Matrix Composites, Springer Science + Business Media, Inc., NY, USA, 2006.
[2] M. Kouzeli, A. Mortensen, Acta Mater. 50 (2002) 39–51.
[3] R.J. Arsenault, L. Wang, C.R. Feng, Acta Metall. Mater. 39 (1991) 47–57.
[4] A. Wanner, D.C. Dunand, Metall. Mater. Trans. 39A (2000) 2949–2962.
[5] M.R. Daymond, C. Lund, M.A.M. Bourke, D.C. Dunand, Metall. Mater. Trans. 30A (1999) 2989–2997.
[6] A.J. Allen, M.A.M. Bourke, S. Dawes, M.T. Hutchings, P.J. Withers, Acta Metall. Mater. 40 (1992) 2361–2373.
[7] M.A.M. Bourke, J.A. Goldstone, N. Shi, J.E. Allison, M.G. Stout, A.C. Lawson, Scr. Metall. Mater. 29 (1993) 771–776.
[8] M.E. Fitzpatrick, M.T. Hutchings, P.J. Withers, Acta Mater. 45 (1997) 4867–4876.
[9] G. Garces, G. Brunno, A. Wanner, Acta Mater. 55 (2007) 5389–5400.
[10] B. Clausen, M.A.M. Bourke, D.W. Brown, E. Üstündag, Mater. Sci. Eng. A A421 (2006) 9–14.
[11] M. Dutta, G. Bruno, L. Edwards, M.E. Fitzpatrick, Acta Mater. 52 (2004) 3881–3888.
[12] A. Pyzalla, J. Nondestruct. Eval. 19 (2000) 21–31.
[13] A. Pyzalla, A. Jacques, J.-P. Feiereisen, T. Buslaps, T. D'Almeida, K.-D. Liss, J. Neutron Res. 9 (2001) 435–442.
[14] E. Maire, A. Owen, J.-Y. Buffiere, P.J. Withers, Acta Mater. 49 (2001) 153–163.
[15] M. Preuss, P.J. withers, E. Maire, J.-Y. Buffiere, Acta Mater. 50 (2002) 3175–3190.
[16] D.K. Balch, D.C. Dunand, Acta Mater. 54 (2006) 1501–1511.
[17] M.L. Young, R. Rao, J.D. Almer, D.R. Haeffner, J.A. Lewis, D.C. Dunand, Acta Mater. 57 (2009) 2362–2375.
[18] S. Roy, J. Gibmeier, A. Wanner A, Adv. Eng. Mater. 11 (2009) 471–477.
[19] G. Requena, G. Garcés, Z. Asghar, E. Marks, P. Staron, P. Cloetens, Adv. Eng. Mater. 13 (2011) 674–684.
[20] S. Roy, J. Gibmeier, V. Kostov, K.A. Weidenmann, A. Nagel, A. Wanner, Acta Mater. 59 (2011) 1424–1435.
[21] B. Huchler, D. Staudenecker, T. Weidler, A. Mattern, A. Nagel, L. Kallien, M. Hoffmann, Proceedings of Symposium Verbundwerkstoffe und Werkstoffverbunde, Frankfurt, Germany, 2005.
[22] C. Genzel, I.A. Denks, J. Gibmeier, M. Klaus, G. Wagener, Nucl. Instrum. Methods Phys. Res. A 578 (2007) 23–33.
[23] E. Macherauch, P. Müller, Z. F. Angew. Phys. 13 (1961) 305–312.
[24] S. Roy, O. Stoll, K.A. Weidenmann, A. Nagel, A. Wanner, Compos. Sci. Technol. 71 (2011) 962–968.
[25] ASM International Handbook Committee, Engineered Materials Handbook. Vol. 1. Composites, ASM International, 1987.
[26] M.R. Daymond, J. Appl. Phys. 96 (2004) 4263–4272.
[27] G.E. Dieter, Mechanical Metallurgy, McGraw-Hill Book Co., UK, 1988.
[28] E. Orowan, Internal Stresses and Fatigue in Metals, Elsevier Publishing Company, New York, 1959.
[29] Z. Wang, R.J. Zhang, Metall. Trans. A 22A (1991) 1585–1593.
[30] Z. Li, S. Schmauder, A. Wanner, Metall. Mater. Trans. A 31A (2000) 2943–2948.
[31] J. Llorca, A. Needleman, S. Suresh, Scr. Metall. Mater. 24 (1990) 1203–1208.
[32] S. Roy, J.M. Gebert, G. Stasiuk, R. Piat, K.A. Weidenmann, A. Wanner, Mater. Sci. Eng. A A528 (2011) 8226–8235.
[33] J. Lemaitre, A Course on Damage Mechanics, Springer, Germany, 1996.
[34] M. Kouzeli, L. Weber, C. San Marchi, A. Mortensen, Acta Mater. 49 (2001) 497–505.
[35] M. Kouzeli, L. Weber, C. San Marchi, A. Mortensen, Acta Mater. 49 (2001) 3699–3709.
[36] J.F. Shackleford, W. Alexander, Materials Science and Engineering Handbook, CRC, Press, Florida, 2001.
[37] Landolt-Börnstein. Band 1. Springer Verlag; 1966.
[38] K.T. Conlon, D.S. Wilkinson, Mater. Sci. Eng. A A317 (2001) 108–114.
[39] S.F. Corbin, D.S. Wilkinson, Acta Metall. Mater. 42 (1994) 1311–1318.
[40] D.J. Lloyd, Acta Metall. Mater. 39 (1991) 59–71.
[41] S.N. Ahmad, J. Hashim, M.I. Ghazali, J. Compos. Mater. 39 (2005) 451–466.
[42] A. Demir, N. Altinkok, Compos. Sci. Technol. 64 (2004) 2067–2074.